

## Contribution of resonance energy transfer to the luminescence quenching of upconversion nanoparticles with graphene oxide

Diego Mendez-Gonzalez<sup>a</sup>, Oscar G. Calderón<sup>b,\*</sup>, Sonia Melle<sup>b</sup>, Jesús González-Izquierdo<sup>c</sup>, Luis Bañares<sup>c</sup>, David López-Díaz<sup>d,g</sup>, M. Mercedes Velázquez<sup>d</sup>, Enrique López-Cabarcos<sup>a</sup>, Jorge Rubio-Retama<sup>a,f</sup>, Marco Laurenti<sup>a,e,f,\*</sup>

<sup>a</sup> Department of Chemistry in Pharmaceutical Sciences, Universidad Complutense de Madrid, 28040 Madrid, Spain

<sup>b</sup> Department of Optics, Universidad Complutense de Madrid, 28037 Madrid, Spain

<sup>c</sup> Department of Physical Chemistry I and Center for Ultrafast Lasers, Universidad Complutense de Madrid, 28040 Madrid, Spain

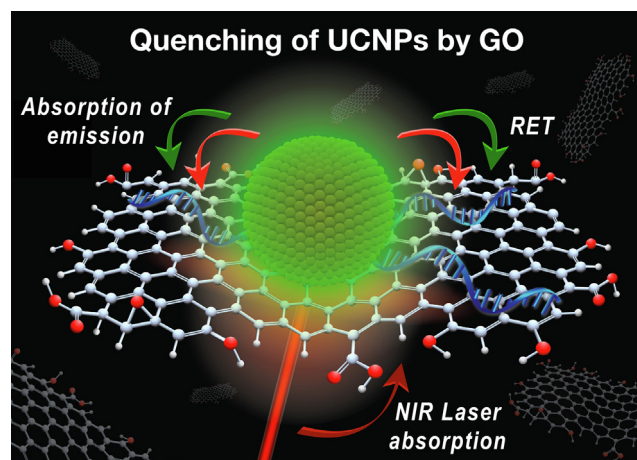
<sup>d</sup> Department of Physical Chemistry, Universidad de Salamanca, 37008 Salamanca, Spain

<sup>e</sup> Instituto de Ciencia de Materiales de Madrid, c/Sor Juana Inés de la Cruz, Cantoblanco 28049, Madrid, Spain

<sup>f</sup> Instituto Ramón y Cajal de Investigación Sanitaria, Hospital Universitario Ramón y Cajal, 28034 Madrid, Spain

<sup>g</sup> Department of Analytical, Physical Chemistry and Chemical engineering, Universidad de Alcalá, 28871 Alcalá de Henares, Madrid, Spain

### GRAPHICAL ABSTRACT



### ARTICLE INFO

#### Article history:

Received 18 February 2020

Revised 31 March 2020

Accepted 19 April 2020

Available online 20 April 2020

#### Keywords:

Graphene oxide

Upconversion nanoparticles

Luminescence quenching

resonance energy transfer (RET)

### ABSTRACT

Upconversion nanoparticles (UCNP) are increasingly used due to their advantages over conventional fluorophores, and their use as resonance energy transfer (RET) donors has permitted their application as biosensors when they are combined with appropriate RET acceptors such as graphene oxide (GO). However, there is a lack of knowledge about the design and influence that GO composition produces over the quenching of these nanoparticles that in turn will define their performance as sensors. In this work, we have analysed the total quenching efficiency, as well as the actual values corresponding to the RET process between UCNPs and GO sheets with three different chemical compositions. Our findings indicate that excitation and emission absorption by GO sheets are the major contributor to the observed luminescence quenching in these systems. This challenges the general assumption that UCNPs luminescence deactivation by GO is caused by RET. Furthermore, RET efficiency has been theoretically calculated by

\* Corresponding authors at: Department of Chemistry in Pharmaceutical Sciences, Universidad Complutense de Madrid, 28040 Madrid, Spain (M. Laurenti).

E-mail addresses: [oscargc@ucm.es](mailto:oscargc@ucm.es) (O.G. Calderón), [marclaur@ucm.es](mailto:marclaur@ucm.es) (M. Laurenti).

Inner filter effect  
Biosensor

means of a semiclassical model considering the different nonradiative energy transfer rates from each  $\text{Er}^{3+}$  ion to the GO thin film. These theoretical results highlight the relevance of the relative positions of the  $\text{Er}^{3+}$  ions inside the UCNPs with respect to the GO sheet in order to explain the RET-induced efficiency measurements.

© 2020 Elsevier Inc. All rights reserved.

## 1. Introduction

Nanoparticles doped with lanthanide ions (Yb, Er, Tm, Ho, etc.) are able to absorb several low energy photons from a continuous-wave (CW) near infrared (NIR) laser and convert them into a fewer number of higher-energy photons that are subsequently emitted as UV/visible light. These nanoparticles are called UCNPs and this feature has been exploited for the development of several different applications spanning from anti-counterfeiting, bioimaging, ultra-sensitive detection of biomolecules (e.g. DNA/RNA), nanothermometers, to other biological and biomedical applications [1–5]. The reason why UCNPs are more attractive than currently used materials in high-sensitivity detection is due to their low photobleaching, blinking, and lack of autofluorescence [6–9].

The detection of biomolecules using luminescence quenching is based on different sensing strategies [10–13]. In general, luminescence quenching can be referred to any process that decrease the emission of a fluorophore, which can occur by a variety of phenomena such as collisional quenching, static quenching, electron transfer, RET, and inner filter effect [14]. Among the different possible luminescence quenching mechanisms, RET is a process that has been widely used to study bio-interactions and for developing biodetection strategies. RET is based on the transfer of energy from a fluorophore in its excited state, which is generally called “donor”, to a nearby **acceptor** in its ground state, called “acceptor”. The nature of this energy transfer is based on donor–acceptor dipole–dipole interactions, and greatly depends on parameters such as dipole to dipole orientation, degree of overlapping between donor emission and acceptor absorption spectra, donor–acceptor distance, quantum efficiency of donor, etc. [15,16] One of the first examples reported in literature regarding the development of a RET-based homogeneous assay using UCNPs as energy donors is the work by Wang et al. [17] In this study the presence of avidin brought in close proximity biotin conjugated UCNPs (i.e. the donors) and Au-biotin nanoparticles (i.e. the acceptors), achieving the quenching of the upconversion luminescence via RET mechanism. Nowadays, researchers have developed many other strategies based on nanomaterials such as gold nanoparticles, carbon nanoparticles, and graphene oxide, among others, which act as energy acceptors into UCNPs-based biosensors [1,2,18,19]. In particular, graphene oxide has emerged as a very promising material to quench the emission of UCNPs for sensing applications [20]. This two dimensional (2D) nanomaterial exhibits a broad absorption spectrum that can quench a wide range of fluorophores like organic dyes, quantum dots or UCNPs [18,21–23]. The accepted detection mechanism is based on the adsorption of single-stranded DNA (ssDNA) modified-UCNPs onto the surface of GO by  $\pi - \pi$  stacking, leading to luminescence quenching. This  $\pi - \pi$  stacking interaction can be avoided or diminished when ssDNA forms double-stranded DNA (dsDNA) upon hybridization or well-folded structures (e.g. ligand recognition by aptamers), as this hampers the interaction between free nucleobases from ssDNA and GO surface [24–28]. This results in a distance change between the UCNPs and the GO surface, which would lead to a restoration of the UCNPs emission. This strategy has been used for the sensitive detection of nucleic acids, proteins, small molecules, and metal ions using UCNPs [18,27,29,30]. These pioneer works have clearly

demonstrated the quenching ability of this 2D nanomaterial, which is achieved thanks to its chemical structure. GO incorporates hydrophilic groups into its structure, which can provide colloidal stability in aqueous solutions and are usually introduced through the chemical oxidation of different types of graphite or carbon nanofibers that are often used as starting raw materials. The most accepted GO structure consists of two different regions of hydrophobic  $\pi$ -conjugated  $\text{Csp}^2$  and hydrophilic  $\text{Csp}^3$  domains, constituted by alcohol and epoxy groups at the basal plane and carboxylic groups at the edges [31,32]. We call the ratio between these two regions  $\beta$ , and it will define its quenching ability [33]. The possibility to systematically modify the chemical composition of GO is interesting for designing DNA/RNA sensors based on RET processes by two main reasons. Firstly, the interaction between the DNA/RNA and graphene oxide can be tuned according to the needs of the sensor. Secondly, the ratio between the  $\text{C}=\text{C}$  groups and  $\text{C}-\text{O}$  and  $\text{COO}^-$  affects the UV–Vis absorption of GO, influencing the spectral overlap and consequently the RET process, as well as its colloidal stability. For this reason, finding optimal GO compositions may improve RET alleviating the relatively low RET efficiency conditioned by the inherently poor quantum yields from the upconversion process [34,35]. Additionally, establishing the full-picture of the UCNPs–GO RET mechanism is of key importance for the rational design of UCNPs–GO systems, especially after witnessing the recent indications that other mechanisms different than RET strongly contribute to luminescence quenching of UCNPs located close to a proper acceptor. For example, Wu et al. have shown that reabsorption is the primary reason for the luminescence quenching of  $\text{NaYF}_4:\text{Yb}^{3+}, \text{Er}^{3+}$  UCNPs encapsulated by an amphiphilic polymer shell containing photoresponsive diarylethene chromophores acting as acceptors [36]. More recently, in a study published by Ding et al., the luminescence quenching of UCNPs encapsulated within Rose Bengal was found to be due to reabsorption (or inner filter effect), being it able to vary between 20% and 93% of the total quenching [37]. Therefore, having a quantitative picture of the roles that RET and inner filter effect play in the UCNPs–GO platform is of paramount importance for rationally constructing efficient RET systems.

In this work, we quantitatively determine the separated contribution of RET and inner filter effect to the global quenching efficiency observed in a donor–acceptor system based on UCNPs and GO pairs. Steady-state and time-resolved luminescence spectroscopy experiments on different GO compositions, and the theoretical modelling reported validate the proposed quenching mechanism. Based on our results, we propose guidelines that may be considered when designing systems based on RET or / and quenching between UCNPs and GO.

## 2. Experimental section

### 2.1. Methods

Transmission electron microscopy (TEM) was used to characterize the UCNPs' size and morphology. TEM grids were prepared by drop-casting of 10  $\mu\text{L}$  of a diluted UCNPs dispersion onto lacey carbon-coated Cu grids, followed by air-drying for 90 s. TEM images were taken on a JEOL JEM-2100 transmission electron

microscope working at 200 kV and equipped with a digital camera GATAN. The nanoparticle size distribution was obtained by means of particle size statistics counting 200 nanoparticles from TEM pictures and using the software FIJI (“Fiji Is Just Image”) v. 2.0.0-rc-59/1.51 k. Powder X-Ray diffraction (XRD) pattern was obtained with a Bruker D8 Advance with Cu K $\alpha$  radiation with rapid detector Lynxeye.

Luminescence spectra of the upconversion nanoparticles were recorded with a home-built system. A pigtailed 10 W CW laser (JDSU, L4-9897603) working at 976 nm was used as excitation source equipped with a digital controller of current and temperature (ILX Lightwave, LDX-36025-12 and LDT-5525B, respectively). The laser beam is transmitted through a long-pass dichroic filter (Semrock, FF757-Di01) and then it is focused on a 1 cm path length cuvette containing the sample with a 10X objective. The upconversion signal coming from the sample is reflected by the dichroic mirror towards a short-pass filter which blocks the IR reflected radiation (Semrock, FF01-775/SP) and, finally, focused into an optical fiber connected to a monochromator (HORIBA Jobin Yvon, iHR320). The monochromator is equipped with a photomultiplier tube (PMT) (Hamamatsu, R928) and uses a 1200 g/mm grating blazed at 900 nm. Three different spectra were taken under the same experimental conditions. Then, the intensity was computed by averaging the value of the integral of each spectral curve within the red emission band, and the maximum deviation was considered as an error. To characterize the laser intensity in the sample, we measured the laser power with a thermal sensor power meter (Thorlabs, S310C) and the beam size using the slit scan technique. The beam waist (half width at half-maximum) is around 150  $\mu$ m and the excitation laser power is 170 mW, leading to a laser irradiance around 240 W/cm<sup>2</sup>. This allows us to ensure that the laser operates well below the excitation saturation intensity of the transition  $^2F_{7/2} \rightarrow ^2F_{5/2}$  for the Yb<sup>3+</sup> ions, which is  $I_{\text{sat}} = \hbar\omega/(2\sigma\tau_{\text{Yb}}) = 3$  kW/cm<sup>2</sup>, where  $\tau_{\text{Yb}} = 2$  ms is the excited level lifetime, and  $\sigma = 1.7 \times 10^{-20}$  cm<sup>2</sup> is the absorption cross-section. We measured the beam divergence along the cuvette path length being the Rayleigh length roughly 1 mm, smaller than the cuvette path length. Optimum luminescence signal was recorded when the beam waist is placed in the first half of the cuvette path length.

Upconversion emission lifetime measurements were obtained using the time-resolved photon counting method. In this experiment, the laser current is modulated to generate excitation pulses of 40  $\mu$ s with a repetition rate of 125 Hz. The luminescence emission at 660 nm is detected by the PMT, which is directly connected (without using a pre-amplifier) to a 50  $\Omega$  input of a digital oscilloscope (Agilent, DSO9104A). The signal from the laser current controller is used to trigger the oscilloscope. We developed a MATLAB program that directly analyses each recorded signal in real-time. This code simulates the discriminator and the multichannel counter. Upon analysis of more than 5000 trigger signals, we obtain a luminescence decay curve. Decay curve measurements were repeated at least three times for each sample under the same experimental conditions.

UV–vis absorbance measurements of the GO samples were performed using a spectrometer (HP 8452) and 1 cm-path length cuvettes. NIR absorbance of the GO samples at 976 nm was measured using a Ge sensor optical power meter from Thorlabs (S122B) and cuvettes with an optical path length of 3 mm.

## 2.2. Materials

Erbium(III) chloride hexahydrate (99.9%), ytterbium(III) chloride hexahydrate (99.9%), yttrium(III) chloride hexahydrate (99.99%), 1-octadecene (80%), oleic acid (90%), sodium hydroxide (98%), ammonium fluoride (98%), methanol (99.9%), *n*-hexane (95%), *N*-(3-(dimethylamino)propyl)-*N'*-ethylcarbodiimide

hydrochloride (EDC) (99%), and *N*-hydroxysulfosuccinimide sodium salt (Sulfo-NHS) (98%), K<sub>2</sub>CO<sub>3</sub> (98%), KMnO<sub>4</sub> (98%), NaIO<sub>4</sub> (99.8%), and DMSO  $\geq$  99.9% were acquired from Sigma-Aldrich. Graphite flakes (99.02% of C) were purchased from Qingdao Super Graphite Co., Ltd. GANF nanofibers have been provided by Carbon Advanced Materials, Grupo Antolín (Burgos, Spain). Commercial GANF<sup>®</sup> fibers consist of a stacked cup of carbon nanofibers composed of graphitic ribbons of approximately five graphene layers. The layers are rolled along the axis of the fiber developing a continuous spiral resulting in a material with a lower number of stacked graphene layers in its structure, thus constituting an excellent starting material to obtain a few layers of graphene oxide. ssDNA sequences 5'-aminohexyl-GGCTTAATCCGACCTGACTTCTG-3' and the same sequence labelled with Cy3 at the 3' end were purchased from ATDBio. All the solvents used in this work were bought from Sigma-Aldrich and used without further purification.

## 2.3. Synthesis of graphene oxides

GO was obtained from two different starting materials such as graphite and carbon nanofibers depending on the desired ratio, which is defined as follows:

$$\beta = \frac{C = C(\%)}{C - O(\%) + COO^-(\%)} \quad (1)$$

A strategy to obtain graphene oxides with different oxidation degrees without using reduction procedures, which often modify the graphene oxide structure by the incorporation of oxidized groups of reductant agents, is to employ different starting materials and to use purification procedures [38–41]. Accordingly, to obtain GO with a  $\beta$  ratio equal to 1 (GO-1), we used as starting material graphite flakes (99.02% of C), while to obtain GO with a  $\beta$  ratio equal to 1.5 (GO-1.5) and  $\beta = 2.6$  (GO-2.6), the starting material was GANF carbon nanofibers. The synthesis procedures were modified Hummer's methods previously reported [39,40]. Finally, to obtain the most reduced graphene oxide ( $\beta = 2.6$ ), we have also employed the purification method reported by Rourke which has been used by our group to produce purified graphene oxides with oxidation degrees similar to those obtained by chemical reduction [42]. X-Ray photoelectron spectroscopy (XPS) demonstrated that graphene oxide synthesized in this work by graphite oxidation (GO-1) contains 51% of C=C, 42% of C–O groups and 7% of carboxylic groups. The chemical composition of GO-1.5 ( $\beta = 1.5$ ) was 61% of C=C, 26% of C–O groups and 14% of COOH groups, while the composition found for GO-2.6 ( $\beta = 2.6$ ) was 72% of C=C, 23% of C–O and 5% of COOH groups [38–41].

## 2.4. Synthesis of NaYF<sub>4</sub>:Yb,Er nanoparticles

The synthesis was performed by following a previously reported procedure [43]. Yttrium(III) chloride hexahydrate (236.6 mg, 0.78 mmol), ytterbium(III) chloride hexahydrate (77.5 mg, 0.20 mmol) and erbium(III) chloride hexahydrate (7.6 mg, 0.02 mmol) were dissolved in a three-necked round bottom flask with a mixture made of 6 mL of oleic acid and 15 mL of 1-octadecene heated at 160 °C for 90 min under a nitrogen atmosphere. After this time and cooling the flask at room temperature, 10 mL of a methanol solution with sodium hydroxide (100 mg, 2.5 mmol) and ammonium fluoride (148.1 mg, 4 mmol) was added dropwise in the reaction under vigorous stirring. This mixture was slowly heated to 100 °C for 30 min with nitrogen atmosphere and then 30 more minutes under vacuum. Finally, the flask was placed in a heating mantle and the temperature was raised to 315 °C for 90 min. The mixture was cooled down to room temperature and the nanoparticles were collected by

centrifugation (8500 rpm, 10 min) with a mixture of hexane, ethanol and water (2:1:1 in volume). The pellet was dispersed with 5 mL of ethanol and centrifuged in a mixture of ethanol and water (1:1 v/v). This process was repeated three times. Finally, the purified NaYF<sub>4</sub>:Yb,Er nanoparticles were dispersed and stored in hexane.

### 2.5. Immobilization of ssDNA chains on the surface of the hydrophilic NaYF<sub>4</sub>:Yb,Er nanoparticles

With the aim of functionalizing the surface of the UCNP with a ssDNA we first performed the Lemieux von Rudloff reaction, where the oleic acid is oxidatively cleaved to form azelaic acid, which has free carboxylic groups that provide colloidal stability and anchoring points for the further functionalization [44]. Briefly, 80 mg of the NaYF<sub>4</sub>:Yb,Er nanoparticles, capped with oleic acid, were dispersed in a solution made by mixing 30 mL of cyclohexane, 21 mL of *tert*-butanol, 9 mL of water and 3 mL of 5% K<sub>2</sub>CO<sub>3</sub>. The resulting mixture was stirred at room temperature for about 20 min. Then, 9 mL of Lemieux-von Rudloff reagent (5.7 mM KMnO<sub>4</sub> and 0.105 M NaIO<sub>4</sub> aqueous solution) was added dropwise and the resulting dispersion was stirred at room temperature for 40 min. The product was then isolated by centrifugation (8500 rpm, 10 min) and washed twice with deionized water and ethanol 1/1. Finally, the DNA was covalently attached to the surface of the nanoparticles by the carbodiimide coupling reaction. In fact the carboxylic acid (–COOH) groups, in the presence of a carbodiimide such as EDC, react with sulfo-NHS resulting in a semi-stable sulfo-NHS ester, which further react with primary amines (–NH<sub>2</sub>) [45]. This reaction produces a covalent bond between the carboxylic acid on the surface of the hydrophilic NaYF<sub>4</sub>:Yb,Er nanoparticles and the primary amino group at the 5' end of the probe ssDNA sequence. To activate the surface carboxylic acid groups, 200  $\mu$ L of EDC 0.2 M and 400  $\mu$ L of sulfo-NHS 0.2 M were added to 3.4 mL of DMSO containing the oxidized NaYF<sub>4</sub>:Yb,Er nanoparticles (4 mg). 60  $\mu$ L of ssDNA 58  $\mu$ M were added to this dispersion and stirred for 18 h at room temperature. After this time the reaction was centrifuged and washed with DMSO for two additional times in order to remove unbound ssDNA.

## 3. Results and discussion

RET is a physical process where the energy of the donor in its excited state is transferred to a proper acceptor that is in the ground state and we prepared donor–acceptor pairs based on UCNP and GO. We used the thermal co-precipitation method at high temperature to synthesize hydrophobic NaYF<sub>4</sub>:Yb,Er

upconverting nanoparticles that are dispersible in organic solvents, due to the presence of oleic acid on their surface acting as capping agent [43]. XRD pattern analysis confirmed that the crystal phase of the synthesized UCNP is hexagonal  $\beta$ -phase, obtained by matching the XRD pattern with the card JCPDS 16-0334 (Fig. S1). The synthesized nanoparticles are monodisperse in size with a diameter of  $32 \pm 4$  nm (Fig. 1A), and show high crystallinity as can be observed in the high-resolution TEM (HR-TEM) in which the measured interplanar spacing of 0.52 nm was indexed to (1 0 0) plane of the hexagonal NaYF<sub>4</sub> crystal (Fig. 1B) [46]. In order to obtain the highest RET efficiency between the different synthesized GOs and the UCNP, we minimized the distance between the donor (UCNP) and the acceptor (GO) by submitting the UCNP to an oxidative cleavage of the oleic acid that yields azelaic acid as capping agent [44]. The free carboxylic groups on the surface of the nanoparticles confer aqueous stability as well as anchoring points for the ssDNA chains. The presence of these groups gives a Z-potential value of  $-24$  mV.

The upconversion emission obtained after exciting an aqueous dispersion of NaYF<sub>4</sub>:Yb,Er nanoparticles with a 976 nm continuous wave laser showed the characteristic green emission peaks at 534 nm and 549 nm (corresponding to transitions  $^2H_{11/2} \rightarrow ^4I_{15/2}$  and  $^4S_{3/2} \rightarrow ^4I_{15/2}$ , respectively), and the red emission peak at 654 nm (corresponding to transition  $^4F_{9/2} \rightarrow ^4I_{15/2}$ ) (Fig. S2). The immobilization of the ssDNA on the surface of the UCNP was carried out by using the NHS/EDC coupling method, which creates an amide bond between the carboxylic group of the azelaic acid and the amine of the 5' end of the ssDNA (i.e., NH<sub>2</sub>-ssDNA). The coupling between NH<sub>2</sub>-ssDNA and UCNP was successfully confirmed (see section S2 in the Supplementary Material). Once the surface of the NaYF<sub>4</sub>:Yb,Er nanoparticles are functionalized with ssDNA strands the nanoparticles are able to interact with the surface of the different GOs. It is well-known that ssDNA interacts noncovalently with 2D nanostructures such as single-walled nanotubes or GO [47–49]. The ssDNA molecules interact with the surface of those nanostructures by means of  $\pi$ -stacking interaction between the nucleotide bases and the conjugated C–C structure of the GO. Hydrogen bonding can also take place between the nucleotide bases and the acceptor moieties from alcohols, ethers, carboxylic and carboxylate oxygen bearing moieties that make the interaction stronger [25]. Double-stranded DNA (dsDNA) has also been proposed to interact with this kind of nanomaterials. However, dsDNA affinity is significantly lower than the affinity of ssDNA [49,50]. This difference in the binding interaction is the base for the use of GO in molecular recognition as well as for the development of biosensors. As a result of these interactions, the UCNP are brought in close proximity to the GO surface and the emission of the NaYF<sub>4</sub>:Yb,Er nanoparticles is quenched. GO is an efficient luminescence

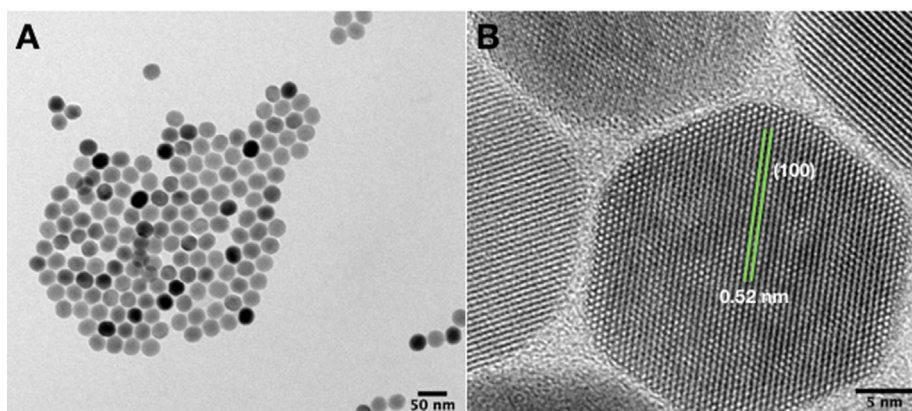


Fig. 1. (A) TEM and (B) HR-TEM micrographs showing monodisperse NaYF<sub>4</sub>:Yb,Er nanoparticles with high crystallinity.

quencher for a variety of fluorophores via non-radiative resonant energy transfer from the fluorophore to GO. Its large absorption cross section and wide absorption spectra enables a large spectral overlap, making GO a suitable and versatile candidate acceptor for different RET biosensors. In our study, we started by characterizing the optical properties of the three synthesized aqueous suspensions of GO (GO-1, GO-1.5, and GO-2.6), acquiring the UV–vis spectra at different concentrations, as shown in Fig. 2A, B, and C.

It is well-established that the UV spectrum of GO exhibits two characteristic bands that can be used to estimate the oxidation degree of graphitic samples. GO-1 presents one main peak between 220 and 230 nm that arises from the  $\pi-\pi^*$  transition of the C=C bonds of the  $sp^2$  regions, and a shoulder around 260 nm due to  $n-\pi^*$  transitions of the C=O and C–O bonds of the  $sp^3$  regions (Fig. 2A). As can be seen from Fig. 2B and 2C the main absorption peak is red shifted when increasing the GO oxidation degree ( $\beta$  ratio). This shift is due to the restored electronic conjugation, at least to some extent, within the carbon framework of the GO sheets upon their reduction [51,52]. GO-2.6 shows a significant decrease in the intensity of the main peak with a concomitant increase of the absorbance for the whole range of wavelengths. Such change is probably due to the aggregation experienced by GO-2.6 because of the augmented graphene character and the lower Z potential exhibited by this GO, being the Z-pot –17 mV for GO-2.6, –31 mV for GO-1.5, and –37 mV for GO-1. The linear absorption coefficient of these GOs samples at 660 nm has been determined following the Lambert-Beer law. The values obtained (see Fig. 2D) agree with typical values found in previous works [53,54]. The above results would seem to indicate that the inner filter effect could have a tremendous impact on the measured upconverting emission intensity during the quenching experiments,

hiding the possible impact of the energy transfer mechanism over the luminescence quenching. For this reason, the UCNPs luminescence quenching induced by the three GOs (GO-1, GO-1.5, and GO-2.6) was measured. Fig. 3A shows the red band upconversion luminescence spectra in absence of GO, as a reference (black line), and after adding 0.2 mg/mL of the different GOs. A huge luminescence decrease is observed, being higher for the more reduced GO sample (GO-2.6). Left axis in Fig. 3B shows the luminescence intensity of the samples containing GO,  $I_{GO}$  (calculated by integrating the UCNPs luminescence spectrum in the presence of GO) normalized to the reference,  $I_0$  (i.e. integrated luminescence spectrum of UCNPs alone), as a function of the  $\beta$  ratio. We also calculated the luminescence quenching efficiency (shown on the right axis of Fig. 3B) as

$$E = 1 - \frac{I_{GO}}{I_0} \quad (2)$$

GO-2.6 has the highest luminescence quenching with a value of 96%, while graphene oxide with a  $\beta$  ratio of 1.5 quenched 85% of the initial emission and GO-1 quenched 64%. Increasing the amount of C hybridised as  $sp^2$ , and as a consequence the  $\pi-\pi$  electrons, translates in a larger quenching. These results suggest that two effects may be favoured when increasing the  $\beta$  ratio: First, more  $\pi-\pi$  stacking interactions between the ssDNA free nucleobases and GO will increase the RET efficiency, as more ssDNA-UCNPs would be adsorbed. Second, greater absorption at 660 nm, as obtained for higher  $\beta$  ratios, will increase RET efficiency since higher values of the overlap integral between the donor (UCNP) and the acceptor (GO) absorption spectra are obtained. Fig. 3C shows the luminescence quenching efficiency achieved at different GO concentrations. A strong increase of quenching efficiency with

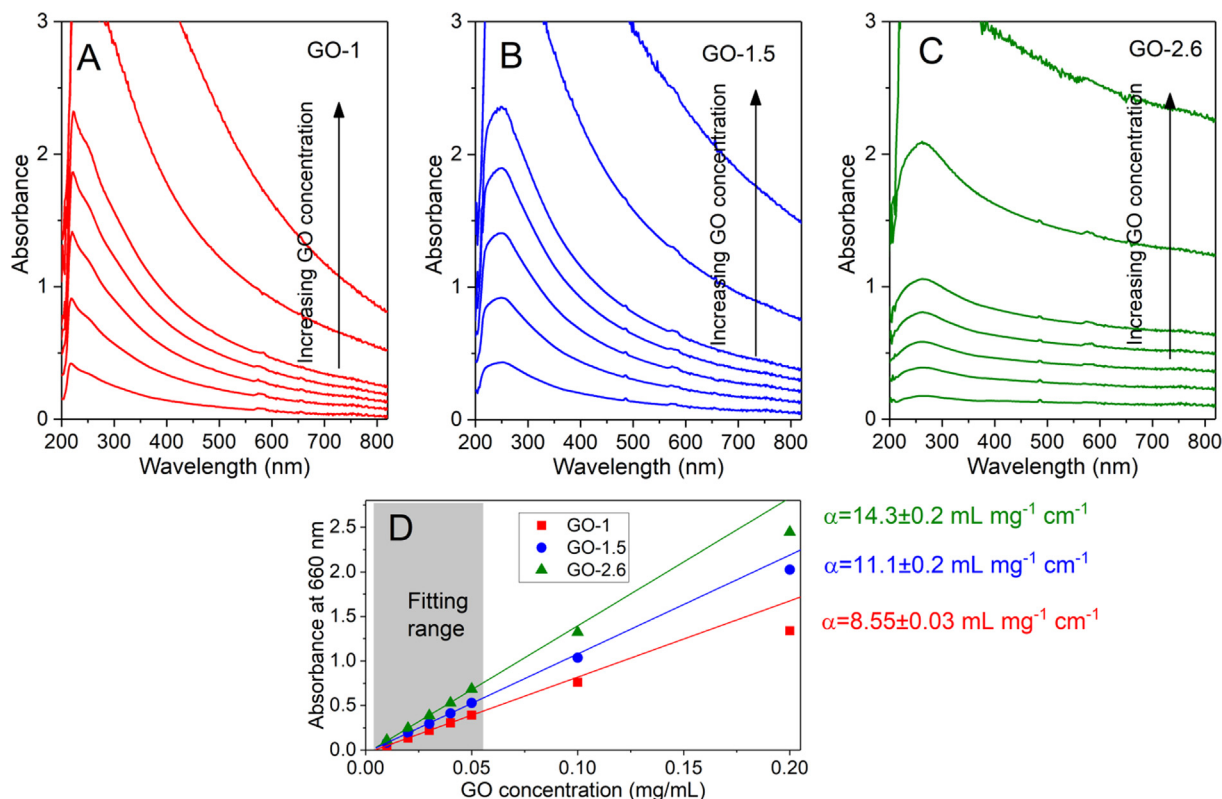


**Fig. 2.** UV–vis absorbance spectrum of aqueous GO suspensions with different  $\beta$  ratios. (A)  $\beta = 1$  (GO-1), (B)  $\beta = 1.5$  (GO-1.5), and (C)  $\beta = 2.6$  (GO-2.6) at concentrations of 0.01, 0.02, 0.03, 0.04, 0.05, 0.1, and 0.2 mg/mL. The measurements were carried out in a 1 cm path length cuvette. The arrow indicates the direction of the GO concentration increase. (D) Absorbance of GO aqueous suspensions at 660 nm as a function of GO concentration. Grey region shows the range of GO concentrations used for the fitting to determine the linear absorption coefficients.

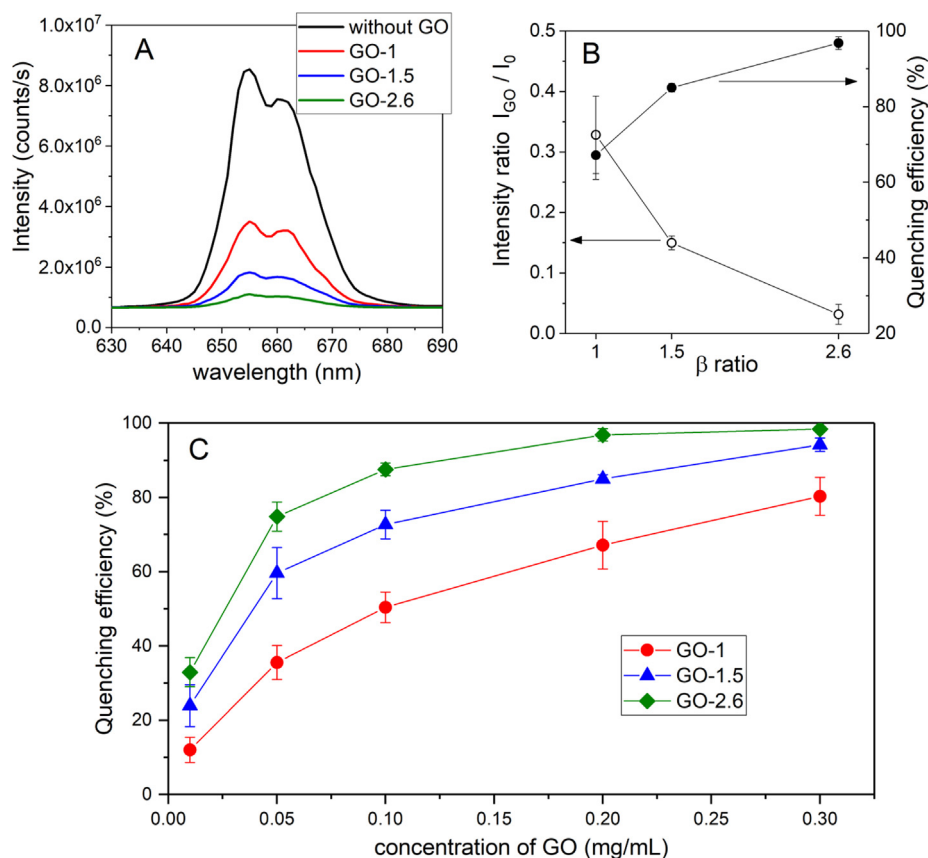


**Fig. 3.** (A) Luminescence emission (red band) of UCNPs in H<sub>2</sub>O (0.1 mg/mL) without GO (black line) and with 0.2 mg/mL of GO-1 (red line), 0.2 mg/mL of GO-1.5 (blue line), and 0.2 mg/mL of GO-2.6 (green line). (B) Luminescence intensity normalized with the reference one (left axis); and luminescence quenching efficiency calculated using Eq. (2) (right axis) as a function of  $\beta$  ratio at 0.2 mg/mL of GO. (C) Luminescence quenching efficiency achieved at different GO concentrations. The error bars were obtained through the intensity error computed by the maximum deviation from three different spectra taken under the same experimental conditions. (For interpretation of the references to colour in this figure legend, the reader is referred to the web version of this article.)

concentration is observed up to a concentration of around 0.1 mg/mL, above which a plateau is reached. For all concentrations, GO-2.6 showed the highest quenching. We corroborated that both UCNPs' emission bands, red and green, are affected by the same factor leading to the similar quenching values for the different  $\beta$  ratios (see Section S3, Fig. S3). In this work, we focused on the red emission band.

Quenching efficiency obtained from steady-state luminescence spectra measures the total quenching which, in principle, is not only due to energy transfer processes but also to inner filter effect. In order to evaluate the contribution of RET to the luminescence quenching of UCNPs by GO, we measured the fluorescence lifetimes from the fluorescence decay curves at 660 nm with and without GO. The quenching efficiency was calculated as

$$E = 1 - \frac{\tau_{GO}}{\tau_0} \quad (3)$$

where  $\tau_0$  is the lifetime of the UCNPs red emission in the absence of GO, and  $\tau_{GO}$  is the lifetime when GO is present. The shorter the UCNPs fluorescence lifetime in the presence of GO, the larger the RET, as it would transfer more efficiently its energy to the nearby GO sheet experiencing a faster decay. As an example, Fig. 4A shows the UCNPs luminescence decay signals in the absence (black curve) and presence (green curve) of GO-2.6. A faster UCNPs luminescence decay time is observed when GO is present (see Fig. 4A, inset), due to the RET phenomenon. Lifetimes were obtained by fitting the decay curves to an exponential function (see Fig. S4 in Supplementary Material). Table 1 shows the lifetime of the ssDNA-NaYF<sub>4</sub>:Yb,Er

without GO and after the addition of 0.2 mg/mL of GO with different oxidation ratios; as well as the RET efficiency.

The quenching efficiency calculated from the lifetime (Eq. (3)) was plotted against the GO  $\beta$  ratio in Fig. 4B (squares) showing a higher quenching efficiency as the GO  $\beta$  ratio increases. For comparative purposes, we also plotted in Fig. 4B (circles) the quenching efficiency obtained from the steady-state luminescence spectra (Eq. (2)). These results demonstrate that the RET phenomenon plays only a secondary role within the observed global quenching.

As shown in Fig. 2, GO suspensions present significant absorption along the whole range of scanned wavelengths, especially GO-1.5 and GO-2.6 suspensions. Thus, one would expect a considerable reabsorption of UCNPs' luminescence (red emission around 660 nm in this case). Furthermore, absorption produced by the GO aqueous suspensions at the excitation wavelength could also lead to luminescence quenching. In order to determine the influence of the absorption by GO in the upconverting luminescence quenching, we measured the absorbance at the excitation laser wavelength 976 nm,  $A_{ex}$ , for the three GO aqueous suspensions at a concentration of 0.2 mg/mL (see Fig. 5A). Interestingly, the absorbance is still relatively high at the excitation wavelength, with measured values around 0.1, 0.2, and 0.43 for GO-1, GO-1.5, and GO-2.6, respectively. We have also corroborated that the contribution of the scattering at the excitation wavelength is negligible (see Fig. S5). Note that part of the luminescence quenching measured on Fig. 4B could be due to the reduced number of 976 nm photons able to reach the UCNPs, being this especially relevant for GO-2.6. It is important to note that photon upconversion, energy transfer

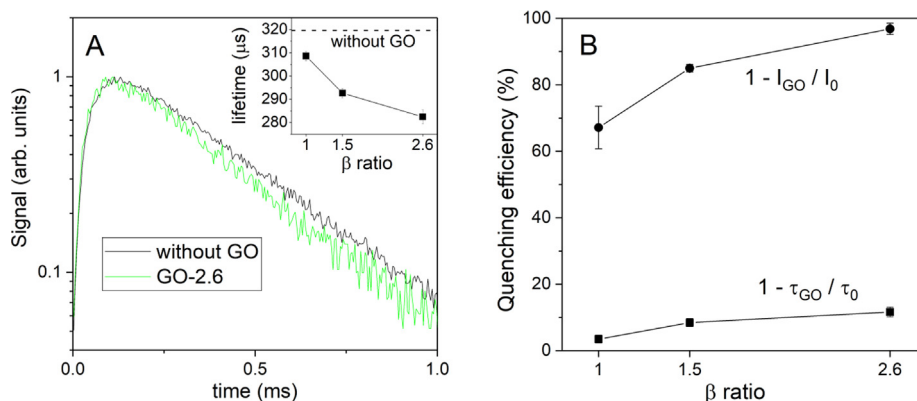


**Fig. 4.** (A) Luminescence decay signal at 660 nm in the absence (black) and presence (green) of GO-2.6 (0.2 mg/mL). (Inset) The lifetime as a function of the GO  $\beta$  ratio. Lifetime error bars are the standard deviation computed from around 35 fits within the same decay curve (see Supplementary Material S4 for fitting procedure). (B) Squares represent the quenching efficiency induced by RET and measured through luminescence decay signals, Eq. (3). Error bars were computed through the lifetime errors. Circles represent the quenching efficiency shown in Fig. 3B measured through the steady-state spectra, Eq. (2). (For interpretation of the references to colour in this figure legend, the reader is referred to the web version of this article.)

**Table 1**

Lifetime of the ssDNA-NaYF<sub>4</sub>:Yb,Er without GO, lifetime of the ssDNA-NaYF<sub>4</sub>:Yb,Er after the addition of 0.2 mg/mL of GO with different oxidation ratios; and RET efficiency obtained from lifetime measurements.

	Without GO	GO-1	GO-1.5	GO-2.6
Lifetime ( $\mu$ s)	319.6 $\pm$ 1.8	308.6 $\pm$ 2.2	292.7 $\pm$ 1.8	282.4 $\pm$ 3.3
RET efficiency (%)		3.5 $\pm$ 1.2	8.4 $\pm$ 1.1	11.6 $\pm$ 1.5

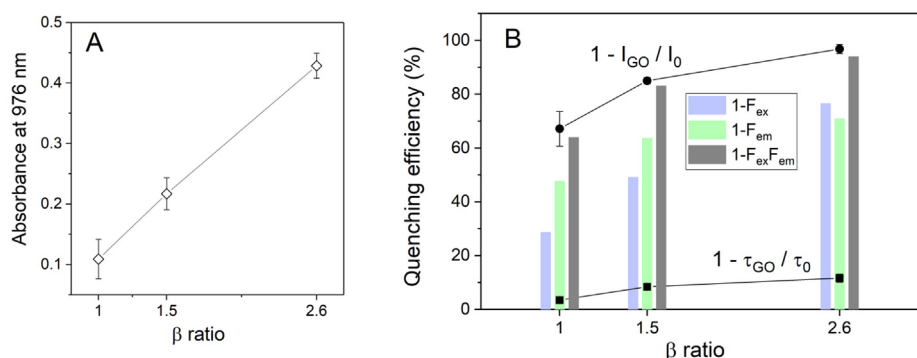


**Fig. 5.** (A) Absorbance at the excitation wavelength (976 nm) of GO aqueous suspensions as a function of the  $\beta$  ratio. The measurements were carried out in a cuvette with 3 mm path length at a GO concentration of 0.2 mg/mL. Error bars correspond to the maximum deviation of three different measurements taken under the same experimental conditions. (B) Quenching efficiency achieved by each one of the two inner filter effects (blue bar: quenching due to absorption of excitation; green bar: quenching due to reabsorption of luminescence emission), and the result of both contributions (grey bar) versus the  $\beta$  ratio. For comparison, the quenching efficiency obtained from the spectra (circles) and decay signals (squares) shown in Fig. 4B are also plotted in this figure. (For interpretation of the references to colour in this figure legend, the reader is referred to the web version of this article.)

upconversion (or ETU) in our case, is a non-linear multi-photon process that can be highly affected by the reduction of the power density pumped to the UCNP. Therefore, the total upconversion luminescence quenching observed in our experiments can be mainly ascribed to three different contributions: the GO absorption of the excitation beam, the GO absorption of the UCNP's luminescence, and the RET phenomenon. Then, the decrease of luminescence can be written as

$$I_{GO}/I_0 = F_{ex}(\eta/\eta_0)F_{em} \quad (4)$$

where the factor  $F_{ex}$  accounts for the excitation beam transmittance through the sample,  $F_{em}$  accounts for the transmittance of the luminescence beam through the sample, and the decrease of intrinsic quantum yield  $\eta/\eta_0$  accounts for the RET to the GO, which decreases the luminescence decay time. All these contributions increase with the  $\beta$  ratio. As a first approach, we estimated the inner

filter contributions by means of the transmittance of the excitation beam and the transmission at the UCNP's red emission wavelength (i.e. 660 nm) through the aqueous GO samples. By using the absorbance at the excitation wavelength of GO samples,  $A_{ex}$ , given in Fig. 5A, we computed the excitation attenuation factor  $F_{ex} = 10^{-(A_{ex}/0.3\text{cm}) \cdot L^2}$  where  $L$  is the distance traveled by the beam inside the sample until its waist. The exponent 2 in  $F_{ex}$  accounts for the quadratic behavior of the upconversion emission with the excitation intensity. This fact, characteristic of upconversion process, makes more relevant the excitation beam absorption in comparison with typical fluorescence processes. By using the GO absorption spectra of Fig. 2 to obtain the absorbance at the UCNP's luminescence red band ( $A_{em}$ ), we computed the emission attenuation factor  $F_{em} = 10^{-(A_{em}/1\text{cm}) \cdot L}$  where the distance travelled by the luminescence inside the sample from the laser waist  $L$  was considered as a fitting parameter. In fact, we obtain a value  $L = 0.22$  cm which

roughly agrees with the beam waist position inside the cuvette observed by eye, as explained in the Experimental Section (Methods). We plotted in Fig. 5B the quenching efficiency achieved by each one of the two inner filter effects and the result of both contributions together, which nearly explain the whole quenching observed in the experiments [55,56].

We found that UCNP-GO as donor–acceptor pair reaches a RET-induced upconversion luminescence quenching with an efficiency of the order of 10%. Although this is a significant value, quenching achieved by RET could be limited by the interplay between the optimum RET distance and the size of the UCNP. In order to theoretically study this point, we estimated the nonradiative energy transfer rate from the UCNP to the GO [57]. We used the RET rate carried out by Gaudreau et al. by means of a semiclassical model which describes the radiated power of a classical dipole emitter (in our case  $\text{Er}^{3+}$  ion) coupled to a nearby thin film (in our case GO). Then, the RET rate from an individual donor  $\text{Er}^{3+}$  ion to an acceptor GO,  $\Gamma_{\text{ET}}^{\text{Er}}$ , is

$$\frac{\Gamma_{\text{ET}}^{\text{Er}}}{\Gamma_0} = \frac{3}{128\pi^3} \text{Im} \left( \epsilon_{\text{GO}} - \frac{1}{\epsilon_{\text{GO}}} \right) t \frac{\lambda^3}{d^4} \quad (5)$$

where  $\Gamma_0$  is the  $\text{Er}^{3+}$  radiative decay rate without GO,  $\lambda$  is the luminescence emission wavelength (660 nm),  $t$  is the thickness of the GO film (in the order of a nanometer),  $\epsilon_{\text{GO}}$  is the permittivity of GO at 660 nm, which should depend on the  $\beta$  ratio, and  $d$  is the distance from the  $\text{Er}^{3+}$  ion under consideration to the GO surface [58,59]. In this expression, we have averaged over all possible dipole orientations with respect to the GO surface. This RET rate exhibits the typical  $d^{-4}$  scaling for thin films. The quenching efficiency  $E^{\text{Er}}$  (i.e. regarding the theoretical quenching by RET) and the intrinsic quantum yield  $\eta^{\text{Er}}$  for each single  $\text{Er}^{3+}$  ion is

$$E^{\text{Er}} = \frac{\Gamma_{\text{ET}}^{\text{Er}}}{\Gamma_{\text{ET}}^{\text{Er}} + 1/\eta_0} \quad (6)$$

$$\frac{\eta^{\text{Er}}}{\eta_0} = \frac{1}{1 + \eta_0 \Gamma_{\text{ET}}^{\text{Er}}} \quad (7)$$

where  $\eta_0$  is the intrinsic quantum yield in absence of GO. We took a value of  $\eta_0 = 0.1$  and a complex refractive index of GO from literature equal to  $n = 1.7$  and  $\kappa = 0.2$  which allows us to determine the GO permittivity [58,59]. We plotted in Fig. 6A both magnitudes,  $E^{\text{Er}}$  (left axis - violet line) and  $\eta^{\text{Er}}$  (right axis - green line), as a function of the ion distance to the GO surface. The distance at which 50% of excited ions are deactivated by RET to GO ( $E^{\text{Er}} = 0.5$ ) is close to 10 nm. Taking into account the size of the UCNP, only a portion of the  $\text{Er}^{3+}$  ions can suffer a significant RET process since most of them are at larger distances. To estimate the global quenching efficiency of the whole UCNP, we averaged the efficiency of each  $\text{Er}^{3+}$  ion inside the nanoparticle.  $N_{\text{Er}}$  is the number of  $\text{Er}^{3+}$  ions inside the nanoparticle given by  $N_{\text{Er}} = f_{\text{Er}} \cdot m \cdot N_A / W = 5719$  where  $W = 20.53$  g/mol is the molar weight of  $\text{NaYF}_4:\text{Yb}/\text{Er}$ , and  $m = (4\pi/3) \cdot a^3 \cdot \rho_{\text{NaYF}_4} = 10^{-16}$  g is the mass of the UCNP, with  $a = 18$  nm the UCNP radius and  $\rho_{\text{NaYF}_4} = 4.2$  g/cm<sup>3</sup> the  $\text{NaYF}_4$  crystal density. The fraction of  $\text{Er}^{3+}$  ions was estimated by the amount of Erbium added to the synthesis being  $f_{\text{Er}} = 0.019$ . This estimation procedure has been validated in a previous work by means of X-Ray energy dispersive spectroscopy measurements [60]. In our model, we generated a uniform random distribution of  $\text{Er}^{3+}$  ions inside the UCNP, which was placed above a GO sheet at a very close distance (2 nm). The distribution of  $\text{Er}^{3+}$  ions (points) inside the UCNP is shown in Fig. 6B. The quenching efficiency of every  $\text{Er}^{3+}$  ion ( $E^{\text{Er}}$ ) is represented by its color (see color bar in Fig. 6). The ions placed very close to the

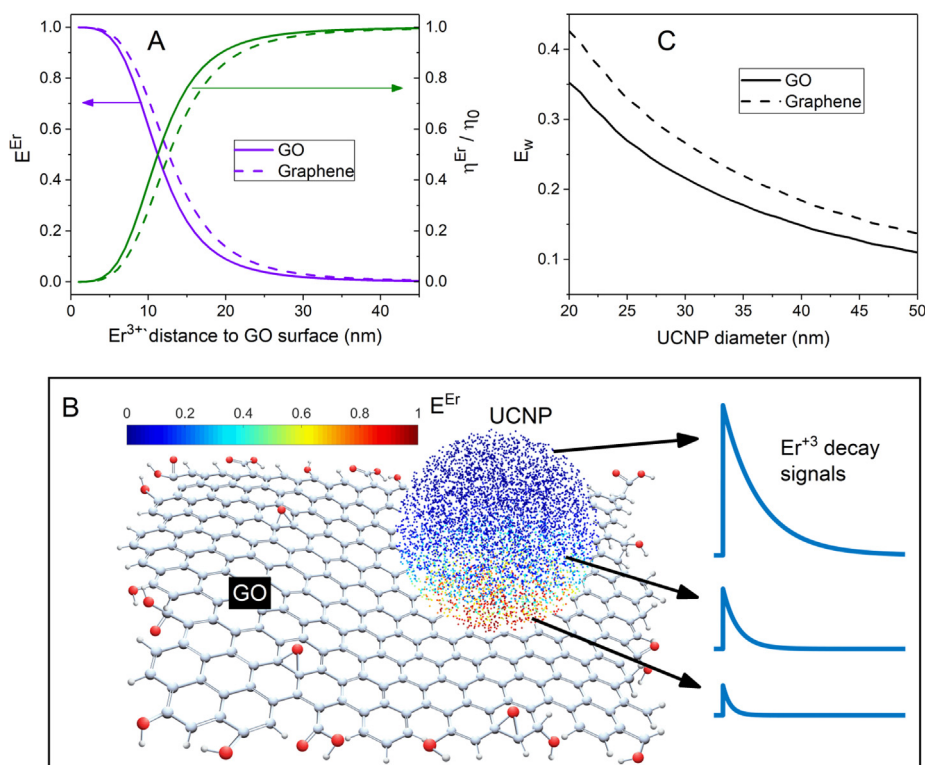


**Fig. 6.** (A) Simulated quenching efficiency (violet line, left axis) and simulated quantum yield (green line, right axis) of an  $\text{Er}^{3+}$  ion as a function of its distance to the GO (solid lines) or to the graphene (dashed line). (B) Simulated distribution of the quenching efficiency of each  $\text{Er}^{3+}$  ion inside the UCNP placed at 2 nm above the GO surface. Blue lines represent luminescence decay signals coming from  $\text{Er}^{3+}$  ions placed at different positions inside the UCNP. (C) Simulated quenching efficiency of the UCNP,  $E_w$ , as a function of the UCNP diameter when interacting with GO (solid line) and graphene (dashed line). (For interpretation of the references to colour in this figure legend, the reader is referred to the web version of this article.)

southern hemisphere suffer a strong quenching, i.e., have a large quenching efficiency. The luminescence decay signals coming from these ions (with faster decays) have a very small amplitude in comparison with the ones coming from the non-affected ions ( $\text{Er}^{3+}$  ions at the north hemisphere), which decay at the original lifetime (see blue lines in Fig. 6B). Therefore, the measurement of the lifetime change in the UCNPs-GO sample should be computed by a weighted average taking into account the individual luminescence intensity of each ion given by  $\eta^{\text{Er}}/\eta_0$ , that is,  $E_w = \frac{(\text{Er}^{\text{Er}})_{N_{\text{Er}}}}{(\eta^{\text{Er}})_{N_{\text{Er}}}}$ , being the value 0.13 which is in good agreement with the values found in the experiments ( $E = 0.116$  or 11.6%).

We found in our experiments that RET increases with  $\beta$  ratio, meaning that a maximum RET efficiency will be obtained in the limit of  $\beta = 100\%$ , i.e., when using graphene. We theoretically calculated the RET rate from an  $\text{Er}^{3+}$  ion to graphene using the work by Gaudreau et al. [57] showing a correlation between RET increase and the  $\beta$  ratio. The RET rate from an  $\text{Er}^{3+}$  ion to graphene can be described following the same previous study:

$$\frac{\Gamma_{\text{ET}}^{\text{Er}}}{\Gamma_0} = \frac{3\alpha}{64\pi^3(\epsilon + 1)^2} \left(\frac{\lambda}{d}\right)^4 \quad (8)$$

where  $\alpha = 1/137$  is the fine-structure constant and  $\epsilon$  is the surrounding medium permittivity. The  $\text{Er}^{3+}$  ion quenching efficiency and intrinsic quantum yield as a function of its distance to graphene are plotted in Fig. 6A (dashed lines). The resulting curves showed similar behavior than the previous analyzed case of GO. In particular, the weighted average quenching efficiency leads to a value of 0.16.

Our results seem to indicate that the size of the UCNPs limits the RET efficiency in this system. A strategy to improve the RET efficiency could be to decrease the UCNPs size. Then, the fraction of active ions that exhibit an efficient energy transfer increases. Let us corroborate this point by using the above theoretical approach. We varied the size of the UCNPs, while keeping the rest of parameters constant. Note that the intrinsic quantum yield  $\eta_0$  of the UCNPs is expected to change with the particle size. Previous studies have found a variation of the total decay rate of the  $\text{Er}^{3+}$  emitting level with the surface area to volume ratio of the UCNPs [61,62]. We used the data measured by Zhao et al. to compute the total decay rate and estimate the variation of the intrinsic quantum yield [63]. We took a radiative decay rate of 2 ms. Fig. 6C shows the quenching efficiency  $E_w$  of the UCNPs as a function of its diameter. The RET increases as the size of the UCNPs decreases. In particular, small UCNPs with diameter around 20 nm would reach a value of  $E_w = 0.35$ . For the sake of completeness, we also plotted  $E_w$  for the case of graphene, which shows a similar behavior but with larger values of  $E_w$  than GO.

#### 4. Conclusions

In this work we have analyzed the different mechanisms that produce quenching of the UCNPs emission by GO. Based in the general assumption that this quenching is mainly governed by RET between the UCNPs and GO, [27,29] we hypothesized that quenching efficiency will depend on GO  $\beta$  ratio compositions (Eq. (1)). Our results demonstrated that the increase of the GO  $\beta$  ratio is accompanied by a corresponding increase in the RET efficiency. However, we have found that the observed luminescence quenching is not only the result of RET from UCNPs (donors) to GO sheets (acceptors), but it is a contribution of several mechanisms that cannot be neglected, namely the absorption of UCNPs excitation and emission by GO due to inner filter effect. Interestingly, RET seems to have the lowest contribution to quenching for all the GO compositions tested, which is a surprising finding when considering that

this system, and the biosensors based on it at similar GO concentrations, are often regarded as sensors based on this phenomenon [18]. The inner filter effect given by GO, especially the absorption of the excitation beam, has a large impact on UCNPs compared with traditional fluorophores, due to the quadratic nature of the upconversion mechanism of red emission [64]. Theoretical analysis of the UCNPs-GO system has revealed that UCNPs' size is the main limitation towards obtaining high RET values, due to the spatial distribution of  $\text{Er}^{3+}$  ions (i.e. emitters) within the UCNPs, which makes them to experience different quenching efficiencies depending on their distance to the GO sheet. The majority of  $\text{Er}^{3+}$  ions are located too far from the GO sheet to be affected by the RET process. Further studies on the optimal distribution of the  $\text{Er}^{3+}$  ions in the UCNPs is underway, in order to maximize the emission quenching by RET aiming to develop more sensitive sensors. Finally, we have drawn the attention to the lifetime measurements, a commonly used technique to characterize energy transfer processes in UCNPs, which should be computed taking into account not only the lifetime of each ion but its individual luminescence intensity.

#### CRediT authorship contribution statement

**Diego Mendez-Gonzalez:** Conceptualization, Investigation, Writing - original draft, Writing - review & editing, Visualization.  
**Oscar G. Calderón:** Conceptualization, Investigation, Software, Writing - original draft, Writing - review & editing, Visualization, Supervision, Funding acquisition.  
**Sonia Melle:** Conceptualization, Investigation, Writing - original draft, Writing - review & editing, Visualization, Supervision, Funding acquisition.  
**Jesús González-Izquierdo:** Investigation, Resources.  
**Luis Bañares:** Investigation, Resources.  
**David López-Díaz:** Investigation, Resources.  
**M. Mercedes Velázquez:** Investigation, Resources, Writing - original draft, Writing - review & editing.  
**Enrique López-Cabarcos:** Resources, Writing - original draft.  
**Jorge Rubio-Retama:** Investigation, Writing - review & editing, Funding acquisition.  
**Marco Laurenti:** Conceptualization, Investigation, Writing - original draft, Writing - review & editing, Supervision, Project administration.

#### Acknowledgements

Grupo Antolín Ingeniería is acknowledged for the generous gift of carbon nanofibers. This work was supported by UCM-Santander (PR26/16-12B), Ministerio de Economía y Competitividad (MAT2014-55065R, MAT2016-75955, and MAT2017-83111R, CTQ2016-78895-R), Ministerio de Ciencia, Innovación y Universidades (RTI2018-094859-B-I00), and Comunidad de Madrid (B2017/BMD-3867 RENIM-CM) co-financed by European Structural and Investment Fund, CTQ2015-65033-P. D. M. G. thanks UCM-Santander for a doctoral contract (CT17/17-CT18/17) and a postdoctoral orientation period "POP" contract. We thank the National Center for Electron Microscopy (CNME), the Center for Ultrafast Lasers (UCM), and COST CM1403. We acknowledge Sara López París (saraparis.design@gmail.com) for her contributions to the figures and artistic works depicted in this publication.

#### Appendix A. Supplementary material

Supplementary data to this article can be found online at <https://doi.org/10.1016/j.jcis.2020.04.076>.

#### References

- [1] G. Chen, H. Qiu, P.N. Prasad, X. Chen, Upconversion nanoparticles: design, nanotechnology, and applications in theranostics, *Chem. Rev.* 114 (2014) 5161–5214.

- [2] H.Q. Peng, L.Y. Niu, Y.Z. Chen, L.Z. Wu, C.H. Tung, Q.Z. Yang, Biological applications of supramolecular assemblies designed for excitation energy transfer, *Chem. Rev.* 115 (2015) 7502–7542.
- [3] D. Yang, P. Ma, Z. Hou, Z. Cheng, C. Li, J. Lin, Current advances in lanthanide ion (Ln)-based upconversion nanomaterials for drug delivery, *Chem. Soc. Rev.* 44 (2014) 1416–1448.
- [4] K. Zhang, Q. Zhao, S. Qin, Y. Fu, R. Liu, J. Zhi, C. Shan, Nanodiamonds conjugated upconversion nanoparticles for bio-imaging and drug-delivery, *J. Colloid Interface Sci.* 537 (2019) 316–324.
- [5] D. Mendez-Gonzalez, S. Lahtinen, M. Laurenti, E. López-Cabarcos, J. Rubio-Retama, T. Soukka, Photochemical ligation to ultrasensitive DNA detection with upconverting nanoparticles, *Anal. Chem.* 90 (2018) 13385–13392.
- [6] G.Y. Chen, J. Shen, T.Y. Ohulchanskyy, N.J. Patel, A. Kutikov, Z.P. Li, J. Song, R.K. Pandey, H. Agren, P.N. Prasad, G. Han, ( $\alpha$ -NaYbF<sub>4</sub>:Tm<sup>3+</sup>)/CaF<sub>2</sub> core/shell nanoparticles with efficient near-infrared to near-infrared upconversion for high-contrast deep tissue bioimaging, *ACS Nano* 6 (2012) 8280–8287.
- [7] G.Y. Chen, T.Y. Ohulchanskyy, W.C. Law, H. Agren, P.N. Prasad, Monodisperse NaYF<sub>4</sub>:Tm<sup>3+</sup>/NaGdF<sub>4</sub> core/shell nanocrystals with near-infrared to near-infrared upconversion photoluminescence and magnetic resonance properties, *Nanoscale* 3 (2011) 2003–2008.
- [8] R. Weissleder, A clearer vision for in vivo imaging, *Nat. Biotechnol.* 19 (2001) 316–317.
- [9] K. Shin, Y.H. Song, Y. Goh, K.T. Lee, Two-dimensional and three-dimensional single particle tracking of upconverting nanoparticles in living cells, *Int. J. Mol. Sci.* 20 (2019) 1424.
- [10] P. Wang, P. Joshi, A. Alazemi, P. Zhang, Upconversion nanoparticle-based ligase-assisted method for specific and sensitive detection of T790M mutation in epidermal growth factor receptor, *Biosens. Bioelectron.* 62 (2014) 120–126.
- [11] D.R. Cooper, K. Kudinov, P. Tyagi, C.K. Hill, S.E. Bradforth, J.L. Nadeau, Photoluminescence of cerium fluoride and cerium-doped lanthanum fluoride nanoparticles and investigation of energy transfer to photosensitizer molecules, *PCCP* 16 (2014) 12441–12453.
- [12] D. Mendez-Gonzalez, E. Lopez-Cabarcos, J. Rubio-Retama, M. Laurenti, Sensors and bioassays powered by upconverting materials, *Adv. Coll. Int. Sci.* 249 (2017) 66–87.
- [13] L. Yan, Y.N. Chang, W. Yin, X. Liu, D. Xiao, L. Zhao, Z. Gu, Y. Zhao, Biocompatible and flexible graphene oxide/upconversion nanoparticle hybrid film for optical pH sensing, *PCCP* 16 (2014) 1576–1582.
- [14] Lakowicz, J. R. *Principles of Fluorescence Spectroscopy*. 2006, Springer, New York, 3rd Edition.
- [15] S. Melle, G.O. Calderón, M. Laurenti, D. Mendez-Gonzalez, A. Egatz-Gómez, E. López-Cabarcos, E. Cabrera-Granado, E. Díaz, J. Rubio-Retama, Förster Resonance Energy Transfer Distance Dependence From Upconverting Nanoparticles To Quantum Dots, *J. Phys. Chem. C* 122 (2018) 18751–18758.
- [16] D. Mendez-Gonzalez, S. Melle, G.O. Calderón, M. Laurenti, E. Cabrera-Granado, A. Egatz-Gómez, E. López-Cabarcos, J. Rubio-Retama, E. Díaz, Control of upconversion luminescence by gold nanoparticle size: from quenching to enhancement, *Nanoscale* 11 (2019) 13832–13844.
- [17] L. Wang, R. Yan, Z. Huo, L. Wang, J. Zeng, J. Bao, X. Wang, Q. Peng, Y. Li, Fluorescence resonant energy transfer biosensor based on upconversion-luminescent nanoparticles, *Angew. Chem. Int. Ed.* 44 (2005) 6054–6057.
- [18] P. Alonso-Cristobal, P. Vilela, A. El-Sagheer, E. Lopez-Cabarcos, T. Brown, O.L. Muskens, J. Rubio-Retama, A.G. Kanaras, Highly sensitive DNA sensor based on upconversion nanoparticles and graphene oxide, *ACS App. Mater. Interfaces* 7 (2015) 12422–12429.
- [19] M. Laurenti, M. Paez-Perez, M. Algarra, P. Alonso-Cristobal, E. Lopez-Cabarcos, D. Mendez-Gonzalez, J. Rubio-Retama, Enhancement of the upconversion emission by visible-to-near-infrared fluorescent Graphene quantum dots for miRNA detection, *ACS App. Mater. Interfaces* 20 (2016) 12644–12651.
- [20] V. Georgakilas, J.N. Tiwari, K.C. Kemp, J.A. Perman, A.B. Bourlino, K.S. Kim, R. Zboril, Noncovalent functionalization of graphene and graphene oxide for energy materials, biosensing, catalytic, and biomedical application, *Chem. Rev.* 116 (9) (2016) 5464–5519.
- [21] F. Li, Y. Huang, Q. Yang, Z. Zhong, D. Li, L. Wang, S. Song, C. Fan, A graphene-enhanced molecular beacon for homogeneous DNA detection, *Nanoscale* 2 (2010) 1021–1026.
- [22] H. Dong, W. Gao, F. Yan, H. Ji, H. Ju, Fluorescence resonance energy transfer between quantum dots and graphene oxide for sensing biomolecules, *Anal. Chem.* 82 (2010) 5511–5517.
- [23] J. Kim, S.J. Park, D.H. Min, Emerging approaches for graphene oxide biosensor, *Anal. Chem.* 89 (2017) 232–248.
- [24] C.H. Lu, H.H. Yang, C.L. Zhu, X. Chen, G.N. Chen, A graphene platform for sensing biomolecules, *Angew. Chem. Int. Ed.* 48 (2009) 4785–4787.
- [25] N. Varghese, U. Mogera, A. Govindaraj, A. Das, P.K. Maiti, A.K. Sood, C.N.R. Rao, Binding of DNA nucleobases and nucleosides with graphene, *ChemPhysChem* 10 (2009) 206–210.
- [26] A.W. Chen, A.L. Briseno, M.M. Santore, Tunable fluorescence quenching near the graphene-aqueous interface, *J. Colloid Interface Sci.* 506 (2017) 76–82.
- [27] D. Giust, M.I. Lucio, A.H. El-Sagheer, T. Brown, L.E. Williams, O.L. Muskens, A.G. Kanaras, Graphene oxide-upconversion nanoparticle based portable sensors for assessing nutritional deficiencies in crops, *ACS Nano* 12 (2018) 6273–6279.
- [28] J.S. Park, N. Goo, D. Kim, Mechanism of DNA adsorption and desorption on graphene oxide, *Langmuir* 30 (2014) 12587–12595.
- [29] C. Zhang, Y. Yuan, S. Zhang, Y. Wang, Z. Liu, Biosensing platform based on fluorescence resonance energy transfer from upconverting nanocrystals to graphene oxide, *Angew. Chem. Int. Ed.* 50 (2011) 6851–6854.
- [30] C. Liu, Z. Wang, H. Jia, Z. Li, Efficient fluorescence resonance energy transfer between upconversion nanophosphors and graphene oxide: a highly sensitive biosensing platform, *Chem. Commun.* 47 (2011) 4661–4663.
- [31] S. Park, R.S. Ruoff, Chemical methods for the production of graphenes, *Nat. Nanotechnol.* 4 (2009) 217–224.
- [32] A. Lerf, H. He, M. Forster, J. Klinowski, Structure of graphite oxide revisited, *J. Phys. Chem. B* 102 (1998) 4477–4482.
- [33] L. Chen, L. Zhang, S. Jiang, Q. Zhang, Mechanistic insights into the fluorescence quenching of rhodamine 6g by graphene oxide, *Chin. J. Chem. Phys.* 31 (2018) 165.
- [34] M.S. Meijer, P.A. Rojas-Gutierrez, D. Busko, I.A. Howard, F. Frenzel, C. Würth, U. Resch-Genger, B.S. Richards, A. Turshatov, J.A. Capobianco, S. Bonnet, Absolute upconversion quantum yields of blue-emitting LiYF<sub>4</sub>:Yb<sup>3+</sup>, Tm<sup>3+</sup> upconverting nanoparticles, *PCCP* 20 (2018) 22556–22562.
- [35] J.C. Boyer, F.C.J.M. van Veggel, Absolute quantum yield measurements of colloidal NaYF<sub>4</sub>:Er<sup>3+</sup>, Yb<sup>3+</sup> upconverting nanoparticles, *Nanoscale* 2 (2010) 1417–1419.
- [36] T. Wu, J.C. Boyer, M. Barker, D. Wilson, N.R. Branda, A “plug-and-play” method to prepare water-soluble photoresponsive encapsulated upconverting nanoparticles containing hydrophobic molecular switches, *Chem. Mater.* 25 (2013) 2495–2502.
- [37] Y. Ding, F. Wu, Y. Zhang, X. Liu, E.M.L.D. de Jong, T. Gregorkiewicz, X. Hong, Y. Liu, M.C.G. Aalders, W. Jan Buma, H. Zhang, Interplay between static and dynamic energy transfer in biofunctional upconversion nanoplateforms, *J. Phys. Chem. Lett.* 6 (2015) 2518–2523.
- [38] R.S. Hidalgo, D. López-Díaz, M.M. Velázquez, Graphene oxide thin films: influence of chemical structure and deposition methodology, *Langmuir* 31 (2015) 2697–2705.
- [39] B. Martín-García, M.M. Velázquez, F. Rossella, V. Bellani, E. Diez, J.L. García Fierro, J.A. Pérez-Hernández, J. Hernández-Toro, S. Claramunt, A. Cirera, Functionalization of reduced graphite oxide sheets with a zwitterionic surfactant, *ChemPhysChem* 13 (2012) 3682–3690.
- [40] D. López-Díaz, M.M. Velázquez, S.B. De La Torre, A. Pérez-Pisonero, R. Trujillano, J.L.G. Fierro, S. Claramunt, A. Cirera, The role of oxidative debris on graphene oxide films, *ChemPhysChem* 14 (2013) 4002–4009.
- [41] D. López-Díaz, M. López Holgado, J.L. García-Fierro, M.M. Velázquez, Evolution of the Raman spectrum with the chemical composition of graphene oxide, *J. Phys. Chem. C* 121 (2017) 20489–20497.
- [42] H.R. Thomas, S.P. Day, W.E. Woodruff, C. Vallés, R.J. Young, I.A. Kinloch, G.W. Morley, J.V. Hanna, N.R. Wilson, J.P. Rourke, Deoxygenation of graphene oxide: reduction or cleaning?, *Chem. Mater.* 25 (2013) 1–16.
- [43] Z. Li, Y. Zhang, An efficient and user-friendly method for the synthesis of hexagonal-phase NaYF<sub>4</sub>:Yb, Er/Tm nanocrystals with controllable shape and upconversion fluorescence, *Nanotechnology* 19 (2008) 345606.
- [44] R. Naccache, F. Vetrone, V. Mahalingam, L.A. Cuccia, J.A. Capobianco, Controlled Synthesis And Water Dispersibility Of Hexagonal Phase NaGdF<sub>4</sub>:Ho<sup>3+</sup>/Yb<sup>3+</sup> nanoparticles, *Chem. Mater.* 21 (2009) 717–723.
- [45] Z. Grabarek, J. Gergely, Zero-length crosslinking procedure with the use of active esters, *Anal. Biochem.* 185 (1990) 131–135.
- [46] H. Chen, Y. Lang, D. Zhao, C. He, W. Qin, Enhanced high-order upconversion luminescence of hexagonal phase NaYF<sub>4</sub>:Yb<sup>3+</sup>, Tm<sup>3+</sup> crystals coated with homogeneous shell, *J. Fluorine Chem.* 174 (2015) 70–74.
- [47] R. Yang, Z. Tang, J. Yan, H. Kang, Y. Kim, Z. Zhu, W. Tan, Noncovalent assembly of carbon nanotubes and single-stranded DNA: an effective sensing platform for probing biomolecular interactions, *Anal. Chem.* 80 (2008) 7408–7413.
- [48] R. Yang, J. Jin, Y. Chen, N. Shao, H. Kang, Z. Xiao, Z. Tang, Y. Wu, Z. Zhu, W. Tan, Carbon nanotube-quenched fluorescent oligonucleotides: probes that fluoresce upon hybridization, *J. Am. Chem. Soc.* 130 (2008) 8351–8358.
- [49] M. Zhang, A. Jagota, E.D. Semke, A. Bruce, B.A. Diner, R.S. Mclean, S.R. Lustig, R. E. Richardson, N.G. Tassi, DNA-assisted dispersion and separation of carbon nanotubes, *Nat. Mater.* 2 (2003) 338–342.
- [50] B. Liu, S. Salgado, V. Maheshwari, J. Liu, DNA adsorbed on graphene and graphene oxide: fundamental interactions, desorption and applications, *Curr. Opin. Colloids Interf. Sci.* 26 (2016) 41–49.
- [51] G. Eda, Y.Y. Lin, C. Mattevi, H. Yamaguchi, H.A. Chen, I.S. Chen, C.W. Chen, M. Chhowalla, Blue photoluminescence from chemically derived graphene oxide, *Adv. Mater.* 22 (2010) 505–509.
- [52] G. Eda, M. Chhowalla, Chemically derived graphene oxide: towards large-area thin-film electronics and optoelectronics, *Adv. Mater.* 22 (2010) 2392–2415.
- [53] Y. Hernandez, V. Nicolosi, M. Lotya, F.M. Blighe, Z.Y. Sun, S. De, I.T. McGovern, B. Holland, M. Byrne, Y. Gunko, et al., High-yield production of graphene by liquid-phase exfoliation of graphite, *Nat. Nanotechnol.* 3 (2008) 563–568.
- [54] M. Lotya, Y. Hernandez, P.J. King, R.J. Smith, V. Nicolosi, L.S. Karlsson, F.M. Blighe, S. De, Z.M. Wang, I.T. McGovern, G.S. Duesberg, J.N. Coleman, Liquid phase production of graphene by exfoliation of graphite in surfactant/water solutions, *J. Am. Chem. Soc.* 131 (2009) 3611–3620.
- [55] S. Chen, Y.-L. Yu, J.-H. Wang, Inner filter effect-based fluorescent sensing systems: a review, *Anal. Chim. Acta* 999 (2018) 13–26.
- [56] Y. Ding, F. Wu, Y. Zhang, X. Liu, E.M.L.D. de Jong, T. Gregorkiewicz, X. Hong, Y. Liu, M.C.G. Aalders, W.J. Buma, H. Zhang, Interplay between static and dynamic energy transfer in biofunctional upconversion nanoplateforms, *J. Phys. Chem. Lett.* 6 (2015) 2518–2523.

- [57] L. Gaudreau, K.J. Tielrooij, G.E.D.K. Prawiroatmodjo, J. Osmond, F.J. de Abajo-García, F.H.L. Koppens, Universal distance-scaling of nonradiative energy transfer to graphene, *Nano Lett.* 13 (2013) 2030–2035.
- [58] I. Jung, M. Vaupel, M. Pelton, R. Piner, D.A. Dikin, S. Stankovich, J. An, R.S. Ruoff, Characterization of thermally reduced graphene oxide by imaging ellipsometry, *J. Phys. Chem. C* 112 (2008) 8499–8506.
- [59] H. Yang, H. Hu, Y. Wang, T. Yu, Rapid and non-destructive identification of graphene oxide thickness using white light contrast spectroscopy, *Carbon* 52 (2013) 528–534.
- [60] G. Mendez-Gonzalez, M. Laurenti, A. Latorre, A. Somoza, A. Vazquez, A.I. Negrodo, E. López-Cabarcos, O.G. Calderón, S. Melle, J. Rubio-Retama, Oligonucleotide sensor based on selective capture of upconversion nanoparticles triggered by target-induced DNA interstrand ligand reaction, *ACS Appl. Mater. & Interfaces* 9 (2017) 12272–12281.
- [61] S.F. Lim, W.S. Ryu, R.H. Austin, Particle size dependence of the dynamic photophysical properties of NaYF<sub>4</sub>:Yb, Er nanocrystals, *Opt. Express* 18 (2010) 2309–2316.
- [62] X. Xue, S. Uechi, R.N. Tiwari, Z. Duan, M. Liao, M. Yoshimura, T. Suzuki, Y. Ohishi, Size-dependent upconversion luminescence and quenching mechanism of LiYF<sub>4</sub>:Er<sup>3+</sup>/Yb<sup>3+</sup> nanocrystals with oleate ligand adsorbed, *Opt. Mater. Express* 3 (2013) 989–999.
- [63] J. Zhao, Z. Lu, Y. Yin, C. McRae, J.A. Piper, J.M. Dawes, D. Jin, E.M. Goldys, Upconversion luminescence with tunable lifetime in NaYF<sub>4</sub>:Yb, Er nanocrystals: role of nanocrystal size, *Nanoscale* 5 (2013) 944–952.
- [64] H. Schäfer, M. Haase, Upconverting nanoparticles, *Angew. Chem. Int. Ed.* 50 (2011) 5808–5829.